

# Constraining Galactic dark matter with gamma-ray pixel counts statistics

H.-S. Zechlin\*

*Istituto Nazionale di Fisica Nucleare, Sezione di Torino, via P. Giuria, 1, I-10125 Torino, Italy*

S. Manconi<sup>†</sup> and F. Donato<sup>‡</sup>

*Dipartimento di Fisica, Università di Torino, via P. Giuria, 1, I-10125 Torino, Italy and  
Istituto Nazionale di Fisica Nucleare, Sezione di Torino, via P. Giuria, 1, I-10125 Torino, Italy*

Gamma-ray searches for new physics such as dark matter are often driven by investigating the composition of the extragalactic gamma-ray background (EGB). Classic approaches to EGB decomposition manifest in resolving individual point sources and dissecting the intensity spectrum of the remaining unresolved component. Furthermore, statistical methods have recently been proven to outperform the sensitivity of classic source detection algorithms in finding point-source populations in the unresolved flux regime. In this article, we employ the 1-point photon count statistics of eight years of *Fermi*-LAT data to resolve the population of extragalactic point sources and to decompose the diffuse isotropic background contribution for Galactic latitudes  $|b| \geq 30^\circ$ . We use three adjacent energy bins between 1 and 10 GeV. For the first time, we extend the analysis to incorporate a potential contribution from annihilating dark matter smoothly distributed in the Galaxy. We investigate the sensitivity reach of 1-point statistics for constraining the thermally-averaged self-annihilation cross section  $\langle\sigma v\rangle$  of dark matter, using different template models for the Galactic foreground emission. Given the official *Fermi*-LAT interstellar emission model, we set upper bounds on the DM self-annihilation cross section  $\langle\sigma v\rangle$  that are comparable with the constraints obtained by other indirect detection methods, in particular by the stacking analysis of several dwarf spheroidal galaxies.

PACS numbers: 95.35.+d,95.75.-z,95.75.Mn,95.85.Pw

## I. INTRODUCTION

The Large Area Telescope (LAT; [1, 2]) on board the *Fermi* Gamma-ray Space Telescope (*Fermi*) has led to tremendous progress in understanding the nature of non-thermal gamma rays reaching the Earth. In general, the all-sky gamma-ray emission is composed of two contributions: a bright foreground produced in our own Galaxy, and all other gamma rays originating from farther sources outside the Galaxy. The latter contributions mutually accumulate to the extragalactic gamma-ray background (EGB, see [3]). The EGB itself disseminates into point sources (PSs) and an effectively isotropic diffuse background contribution, the IGRB. At Galactic latitudes  $|b| > 20^\circ$ , the EGB has been detected with the LAT between 100 MeV and 820 GeV with unprecedented precision [4].

Blazars represent the brightest and most numerous source population among all sources resolved in the EGB (e.g., [5–9]). In addition, gamma-ray source catalogs such as the *Fermi* Large Area Telescope Third Source Catalog (3FGL; [10]) list associations of gamma-ray sources with other source types, among them misaligned active galactic nuclei and star-forming galaxies (see [11] and references therein). Different source populations distinguish themselves observationally by spectral and tempo-

ral characteristics. Another population intrinsic quantity is their source count distribution  $dN/dS$ , denoting the number of sources  $N$  per solid angle element  $d\Omega$  with integral fluxes in the interval  $(S, S + dS)$ . The phenomenology of  $dN/dS$  distributions can be obtained from specific, mostly data-driven models, derived from basic principles of source-intrinsic gamma-ray production and cosmological source evolution. The extrapolation of these models suggests the existence of numerous sources with fluxes fainter than current source detection thresholds [9, 12–17]. Thus, the IGRB is expected to originate at least partly from unresolved faint point-source populations. As opposed to source contributions, the IGRB might contain purely diffuse components, among them diffuse gamma rays originating from cosmic-ray interactions with the intergalactic medium [4] or the annihilation or decay of dark matter (DM) particles in the Milky Way’s halo and halos of outer galaxies. To that regard, the IGRB serves as a complementary probe for Galactic and cosmological DM [18–23].

Singling out a possible DM contribution to the IGRB usually is complicated by a number of uncertainties: The modeling of Galactic diffuse foreground emission, the uncertain contribution from unresolved sources, and the accuracy of model predictions for the DM signal strength itself prevent the IGRB from currently being considered a clean target for DM searches [23, 24]. However, the sensitivity of DM searches in the IGRB with *Fermi*-LAT data has been demonstrated to reach competitive limits, for example with respect to recent dwarf spheroidal galaxy observations [22–24]. In the near future, both im-

\* zechlin@to.infn.it

† manconi@to.infn.it

‡ donato@to.infn.it

improvements of the LAT sensitivity for detecting point-like sources and various attempts of reducing systematic model uncertainties with complementary observations will consolidate the crucial role of the IGRB in DM searches.

The dissection of the EGB by means of individual source detections and intensity measurements can be complemented by statistical methods. Analyses employing statistical properties of the observed counts map have been demonstrated to be capable of measuring  $dN/dS$  and the diffuse EGB components [25–33]. We have shown in Refs. [33] and [34] (henceforth Z16a and Z16b, respectively) that the 1-point probability distribution function (1pPDF) of counts maps serves as a unique tool for precise measurements of  $dN/dS$  and the EGB’s composition. In short, the 1pPDF represents the probability distribution function of photon counts as distributed in a pixelized sky map. Statistical measurements are not only complementary to standard analysis procedures, but they also significantly increase the sensitivity for resolving faint point-source populations.

Searches for DM signals in the EGB with statistical methods such as the 1pPDF will thus particularly profit from a better sensitivity with regard to resolving faint point sources as well as from the unique dissection capabilities in general. In this article, we extend the 1pPDF method presented in Z16a,b to incorporate an additional component representing a smooth Galactic DM halo. We further investigate the achievable sensitivity reach of the 1pPDF method with regard to constraining the DM self-annihilation cross section  $\langle\sigma v\rangle$ , on the basis of eight years of *Fermi*-LAT data between 1 and 10 GeV and different Galactic foreground emission models. Our exploration is meant as a sensitivity study to seek diffuse photons originating from DM annihilation at high Galactic latitudes. Since the 1pPDF method incorporates both resolved and unresolved point sources, source locations do not have to be excluded from the data and results can be considered as catalog independent.

The 1pPDF method and the modeling of the gamma-ray sky (including the DM component) are discussed in Section II. *Fermi*-LAT data reduction and the data analysis setup are discussed in Section III. Section IV focuses on the actual 1pPDF analysis, while results are discussed in Section V. The paper concludes with Section VI.

## II. THE 1PPDF METHOD AND DM

The mathematical foundations of the 1pPDF method, the implementation, and the application of the method to *Fermi*-LAT data are discussed in Z16a,b. In this article, we extend the model of the gamma-ray sky to an additional component, i.e. the total gamma-ray emission is described by superimposing four different contributions:

1. An isotropic distribution of gamma-ray point sources, described with a differential source-count distribution  $dN/dS$ . The  $dN/dS$  distribution is

parameterized with a multiply broken power law (MBPL), with its free fit parameters comprising the overall normalization, a number of  $N_b$  break positions, and therefore  $N_b + 1$  power-law components connecting the breaks.

2. A diffuse component of Galactic foreground emission, described with an interstellar emission model (IEM). Further details on the considered IEMs are given in Section II A. The global normalization of the IEM template is kept a free fit parameter,  $A_{\text{gal}}$ .
3. A diffuse component accounting for all contributions indistinguishable from purely diffuse isotropic emission. The diffuse isotropic background emission is assumed to follow a power law spectrum (photon index  $\Gamma = 2.3$ ), with its integral flux  $F_{\text{iso}}$  serving as the free normalization parameter.
4. A distribution of Galactic DM, representing a typical smooth DM halo. The gamma-ray emission from the DM halo is included as a template with a free global normalization parameter,  $A_{\text{DM}}$ . Details are discussed in Section II B.

In the subsequent paragraphs, the mathematical base of the 1pPDF is briefly revisited. The reader is referred to Z16a, Section 2, for details.

Let  $\mathcal{P}^{(p)}(t)$  be a probability generating function of a discrete probability distribution  $p_k^{(p)}$ , where  $t \in \mathbb{R}$  is an auxiliary variable,  $k = 0, 1, 2, \dots$  is a discrete random variable, and  $p$  denotes the evaluated map pixel  $p$ . Then  $p_k^{(p)}$  is given by

$$p_k^{(p)} = \frac{1}{k!} \left. \frac{d^k \mathcal{P}^{(p)}(t)}{dt^k} \right|_{t=0}. \quad (1)$$

The generic representation of the generating function for photon count maps can be derived from a superposition of Poisson processes:

$$\mathcal{P}^{(p)}(t) = \exp \left[ \sum_{m=1}^{\infty} x_m^{(p)} (t^m - 1) \right], \quad (2)$$

where  $x_m^{(p)}$  is the expected number of point sources per pixel  $p$  that contribute exactly  $m$  photons to the total pixel photon content. The quantity  $x_m^{(p)}$  is therefore given by the source-count distribution  $dN/dS$ , where  $S$  denotes the integral photon flux of a source in the energy band  $[E_{\text{min}}, E_{\text{max}}]$ , i.e.

$$x_m^{(p)} = \Omega_{\text{pix}} \int_0^{\infty} dS \frac{dN}{dS} \frac{(\mathcal{C}^{(p)}(S))^m}{m!} e^{-\mathcal{C}^{(p)}(S)}, \quad (3)$$

where  $\mathcal{C}^{(p)}(S)$  denotes the average number of photons contributed to pixel  $p$  by a source with flux  $S$ , and  $\Omega_{\text{pix}}$  is the solid angle of the pixel. Diffuse background components can be represented by 1-photon source terms, i.e.

$$\mathcal{D}^{(p)}(t) = \exp \left[ x_{\text{diff}}^{(p)} (t - 1) \right], \quad (4)$$

where  $x_{\text{diff}}^{(p)}$  denotes the number of diffuse photon counts expected in map pixel  $p$ . The total generating function then factorizes in the point-source component and the diffuse component,

$$\mathcal{P}^{(p)}(t) = \mathcal{P}_S^{(p)}(t) \mathcal{D}^{(p)}(t). \quad (5)$$

For our model of the gamma-ray sky, the total diffuse contribution  $x_{\text{diff}}^{(p)}$  is given by

$$x_{\text{diff}}^{(p)} = A_{\text{gal}} x_{\text{gal}}^{(p)} + A_{\text{DM}} x_{\text{DM}}^{(p)} + \frac{x_{\text{iso}}^{(p)}}{F_{\text{iso}}} F_{\text{iso}}, \quad (6)$$

where  $x_b^{(p)}$ , with  $b \in \{\text{gal}, \text{DM}, \text{iso}\}$ , reads

$$x_b^{(p)} = \int_{\Omega_{\text{pix}}} d\Omega \int_{E_{\text{min}}}^{E_{\text{max}}} dE f_b^{(p)}(E) \mathcal{E}^{(p)}(E), \quad (7)$$

with  $f_b^{(p)}(E)$  being the differential flux as function of the energy  $E$ , and  $\mathcal{E}^{(p)}(E)$  the pixel-dependent exposure of the detector.

The likelihood function is given by a product over the probabilities  $P$  of finding the number  $k_p$  of measured counts in pixel  $p$ . With the probability  $P(k_p)$  directly given by Eq. 1, the total likelihood of the region of interest (ROI), covered by  $N_{\text{pix}}$  pixels, reads

$$\mathcal{L}(\Theta) = \prod_{p=1}^{N_{\text{pix}}} P(k_p) \quad (8)$$

for a given parameter vector  $\Theta$ .

For real data sets, we note that Eq. 3 has to be corrected for source-smearing effects caused by a finite detector point-spread function (PSF). See Z16a for details.

### A. Galactic Foreground Emission

Gamma rays from the interaction of cosmic rays (CRs) with interstellar gas and interstellar radiation fields (IRFs) in our Galaxy are the main contributors to the emission observed with the LAT above 100 MeV and constitute the diffuse Galactic foreground. This emission provides a complementary tool to study the properties of CRs throughout the Galaxy and the interstellar medium, and dominates the emission coming from point sources, extragalactic diffuse contributions, as well as a possible DM signal.

Modeling the diffuse Galactic emission is complex and equipped with high systematic uncertainties. The morphological structure and the spectrum of the Galactic emission are caused by a sum of different contributions, driven by a variety of different physical parameters. The interaction of CRs with the interstellar HI and  $H_2$  gas is responsible for the production of gamma rays through non-thermal bremsstrahlung and  $\pi^0$  production and their

subsequent decay, while the interaction of Galactic electrons with the IRFs produces gamma rays through inverse Compton (IC) scattering. To properly compute these contributions, models for CR sources, injection spectra, and diffusion in our Galaxy, as well as a good understanding of the interstellar gas distribution and the structure of radiation fields are required. The computation of the different components is additionally hampered, for instance, by the presence of large-scale structures correlated to Galactic Loop I [35] or the *Fermi* Bubbles [36], or by well-known degeneracies among propagation parameters.

A search for DM (and other additional components) with methods relying on IEM templates requires a rigorous assessment of possible systematics driven by the IEM. In particular the IC component, which is expected to be a possible cause of degeneracies with the DM component, would need to be freely adjustable by the fit, cf. Ref. [37]. Nevertheless, when considering high latitude regions ( $|b| > 30^\circ$ ) away from the Galactic plane (GP), a representative small set of IEMs may be considered sufficient to quantify uncertainties due to Galactic foreground modeling [4, 38]. To bracket the uncertainties inherent to the IEM we consider 4 different models: Our benchmark IEM adopts the official spatial and spectral template as provided by the *Fermi*-LAT Collaboration for the Pass 8 analysis framework (`gll_iem.v06.fits`, see Ref. [39] and Section III). In addition, we compare analyses using the models A, B, and C as used in Ref. [4] to bracket the systematic uncertainties of the IGRB analysis. The same three models A, B, C have also been used in Refs. [23, 24] to study uncertainties related to the diffuse Galactic emission modeling when searching for DM contributions in the IGRB data. An extended description of the characteristics of the models A, B, C can be found in Appendix A of Ref. [4]. Here, we summarize the main elements and differences between the models, in particular focusing on Galactic latitudes  $|b| > 30^\circ$ .

The A, B, C model templates provided for the emission related to HI +  $H_2$  and IC have been obtained with a modified version of the GALPROP propagation code (see Ref. [4] for details). The main differences between these models regard the IC component and the treatment of CR diffusion. In model B, an additional electron source population near the Galactic Center (GC) produces the bulk of the IC emission. With respect to model A and C, this translates into a better agreement between the template prediction for the IC component and the fit of model B to gamma-ray data for Galactic latitudes  $|b| > 20^\circ$ , see Ref. [4] for details. In fact, we found that the relative difference between the IC component in the energy bin between 1.99 and 5.0 GeV and  $|b| > 30^\circ$  for models A and B is  $(IC_A - IC_B)/IC_A > 0$  for all pixels, ranging from 40% to 70%. The same relative difference between the IC components of models B and C ranges from 60% up to a factor of 2 in the outer Galaxy. Fig. 1 represents the relative difference between the entire emission predicted by model A and B, in the energy bin

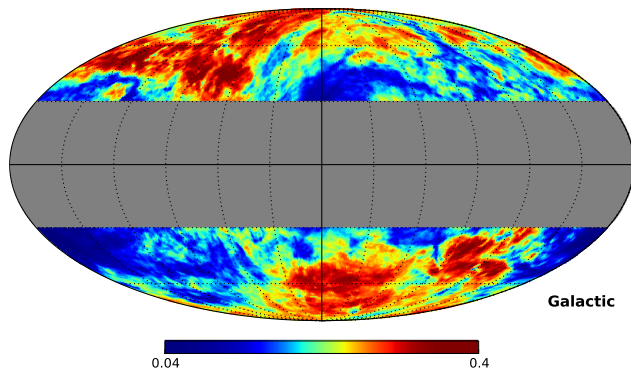


FIG. 1. Relative difference between the Galactic diffuse emission predicted by model A and B, for latitudes  $|b| > 30^\circ$ . Models are taken from Ref. [4] and are integrated in the energy bin between 1.99 and 5.0 GeV. The Mollweide projection is given in Galactic coordinates, centered on the GC. The GP region has been masked in gray.

between 1.99 and 5.0 GeV for latitudes  $|b| > 30^\circ$ . The differences follow the complicated structure of Galactic gas and indicate that model A predicts higher (40% at most) diffuse emission in the whole ROI. In model A and B, the CR diffusion coefficient and re-acceleration strength are constant throughout the Galaxy. In model C, instead, a dependency on the galactocentric radius and height is introduced, causing a more efficient transport of CRs and therefore higher gamma-ray intensities in the outer Galaxy, as shown by Fig. 20 in Ref. [4].

In our analysis, each IEM is re-normalized with an additional global normalization factor  $A_{\text{gal}}$  that is allowed to float freely. We underline that the various models are studied here to explore the effect of changing foreground morphology, in particular of the IC emission, on the contribution from the additional Galactic DM component. A complete study on whether the data prefer one of those models over the other is beyond the scope of this work, and it is extensively addressed for example in Ref. [40].

## B. The DM Component

Based upon the assumption that the building blocks of DM are new fundamental particles, e.g., weakly interacting massive particles (WIMPs), DM can self-annihilate or decay into standard model final states. Gamma-ray photons are then unavoidably produced by secondary processes such as hadronization, the subsequent decay of  $\pi^0$ -mesons, and internal bremsstrahlung, which lead to a continuous gamma-ray spectrum over several decades in energy, as well as direct annihilation into line-like features. The observed differential gamma-ray flux per unit energy interval  $(E, E + dE)$  and solid angle  $d\Omega$  from DM

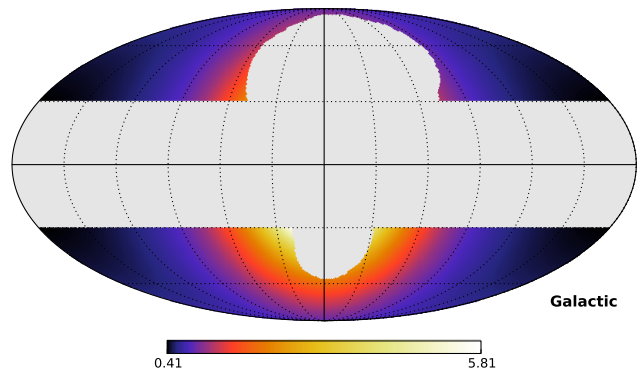


FIG. 2. Dimensionless J-factor for annihilating DM as distributed in the Galaxy following an Einasto profile. The Mollweide projection is given in Galactic coordinates, centered on the position of the GC. The GP and the regions covered by the Fermi Bubbles and Galactic Loop I have been masked in gray, cf. Section IV.

annihilation in a given celestial direction reads

$$\frac{d\phi_{\text{DM}}}{dE d\Omega} = \frac{1}{4\pi} \frac{\langle\sigma v\rangle}{2} r_\odot \frac{\rho_\odot^2}{m_{\text{DM}}^2} \sum_f \left( \frac{dN_f}{dE} B_f \right) \mathcal{J}(\psi). \quad (9)$$

The quantity  $\langle\sigma v\rangle$  resembles the thermally-averaged self-annihilation cross section times the relative velocity,  $m_{\text{DM}}$  denotes the DM particle mass, and  $r_\odot = 8.5$  kpc and  $\rho_\odot = 0.4$  GeV cm $^{-3}$  [41, 42] are normalization constants, i.e. the galactocentric Solar distance and the DM density at  $r_\odot$ , respectively. Equation 9 is valid for self-conjugated DM particles. The differential gamma-ray spectrum yielded by DM annihilation into the standard model final state  $f$  with branching ratio  $B_f$  is given by  $dN_f/dE$ . The dimensionless J-factor reads

$$\mathcal{J}(\psi) = \frac{1}{r_\odot} \int_{\text{los}} \left( \frac{\rho[r(l)]}{\rho_\odot} \right)^2 dl(\psi). \quad (10)$$

Here,  $\rho(r)$  denotes the DM density profile as a function of the galactocentric radius  $r$ , and the line-of-sight (los),  $l$ , as measured from the Galactic position of the Sun is given by  $r(l, \psi) = \sqrt{r_\odot^2 + l^2 - 2r_\odot l \cos \psi}$ , where  $\psi$  is the angle between the vector pointing to the GC and the direction of observation.

We consider here the contribution from DM annihilation in a smooth Galactic halo. We neglect a possible contribution from Galactic DM subhalos, which can be modeled as point-like or slightly extended sources in almost all relevant DM scenarios [see, e.g., 43–49] and will therefore contribute to the generic  $dN/dS$  component. For the density profile of the smooth Galactic halo, we consider an Einasto profile [50]

$$\rho(r) = \rho_\odot \exp\left(-\frac{2}{\alpha} \frac{r^\alpha - r_\odot^\alpha}{r_s^\alpha}\right), \quad (11)$$

with  $\alpha = 0.17$  and  $r_s = 21.8$  kpc [51]. The dimensionless J-factor template map was generated by solving Eq. 10 independently for each map pixel  $p$ , see Fig. 2. The HEALPix resolution of the template map was chosen corresponding to the resolution used in the data analysis, see Section III.

The quantity  $x_{\text{DM}}^{(p)}$  (see Eq. 6) is given by Eqs. 7 and 9. Here, we assume a benchmark annihilation cross section of  $\langle\sigma v\rangle_0 = 10^{-26} \text{ cm}^3\text{s}^{-1}$ , such that the dimensionless fit parameter  $A_{\text{DM}}$  represents a rescaling of the DM flux provided by Eq. 9, given  $\langle\sigma v\rangle_0$  and the chosen normalization  $\rho_\odot$ . We consider DM annihilation into pure  $b\bar{b}$  quark final states and pure  $\tau^+\tau^-$  lepton final states. Those channels serve as benchmark annihilation channels, bracketing general DM annihilation scenarios. The gamma-ray spectra emerging from the final states were taken from Ref. [52]. Possible secondary IC emission from the scattering of charged light leptons with IRFs was neglected [21]. The peak of the energy spectra  $E^2 dN/dE$  usually scales with the DM particle mass,  $E_{\text{peak}} \propto m_{\text{DM}}$ , implying that the best choice for the energy bin to analyze can depend on the DM mass. We investigated DM particles with masses between 5 GeV and 1 TeV.

### III. FERMI-LAT DATA REDUCTION

We processed all-sky *Fermi*-LAT gamma-ray data that were taken within the first 8 years of the mission, i.e. from 2008 August 4 (239,557,417 s MET) through 2016 August 4 (492,018,220 s MET). We used `Pass 8` data [53] along with the corresponding instrument response functions. The Fermi Science Tools (v10r0p5, released date 2015 June 24) [54] were employed for event selection and data processing.

To reduce systematic uncertainties, the 1pPDF analysis requires clean data sets with low residual cosmic-ray backgrounds and event samples exhibiting comparably mild PSF smoothing effects (see Z16a,b). We therefore only used events passing the most stringent `Pass 8` data classification criteria, i.e. belonging to the `ULTRACLEANVETO` event class. The corresponding instrument response functions `P8R2_ULTRACLEANVETO_V6` were used. Furthermore, we restricted the event sample to the PSF3 quartile, to avoid significant PSF smoothing. A possible contamination from the Earth's limb was reduced by restricting the zenith angle to a maximum of  $90^\circ$ . The data selection referred to standard quality selection criteria (`DATA_QUAL==1` and `LAT_CONFIG==1`), and the rocking angle of the satellite was constrained to values smaller than  $52^\circ$ .

To maximize the sensitivity for the  $m_{\text{DM}}$  parameter space (see Section II B), we chose to analyze three adjacent energy bands: (i) 1.04–1.99 GeV, (ii) 1.99–5.0 GeV, and (iii) 5.0–10.4 GeV. The bands were selected following Z16b. The PSF as a function of energy becomes significantly larger than  $1^\circ$  at energies below  $\sim 1$  GeV, but approaches sizes below  $0.1^\circ$  for energies above  $\sim 10$  GeV.

The effective PSF of each energy band was derived by weighting the PSF with the average exposure  $\mathcal{E}(E)$  of the ROI and power-law-type energy spectra (see Eq. 19 in Z16a). The effective PSF widths corresponding to the three energy bands are (i)  $0.31^\circ$ , (ii)  $0.18^\circ$ , and (iii)  $0.10^\circ$ .

The data were spatially binned using the HEALPix equal-area pixelization scheme [55]. Thus, the entire sky is covered by  $N_{\text{pix}} = 12N_{\text{side}}^2$  pixels, where  $N_{\text{side}} = 2^\kappa$ . We compared two choices for the resolution parameter  $\kappa$  of the pixelization, i.e.  $\kappa = 6$  and  $\kappa = 7$ , approximating the size of the PSF.

### IV. DATA ANALYSIS

The 1pPDF likelihood function  $\mathcal{L}(\Theta)$  as defined in Eq. 8 was analyzed following the method of Z16a. We used the Bayesian Markov Chain Monte Carlo (MCMC) sampler `MultiNest` [56, 57] to sample the posterior distribution  $P(\Theta) = \mathcal{L}(\Theta)\pi(\Theta)/\mathcal{Z}$ , where  $\pi(\Theta)$  is the prior and  $\mathcal{Z}$  is the Bayesian evidence. `MultiNest` was operated in its standard configuration. We used 1000 live points together with a tolerance criterion of 0.2. The configuration was checked for stability. Priors were either log-flat or flat, cf. Z16a, and their ranges were chosen such that to sufficiently cover the posterior distributions. In particular, the newly introduced prior for  $A_{\text{DM}}$  was of the log-flat type.

From the final posterior sample, we built one-dimensional profile likelihood functions [58] for each parameter, in order to get prior-independent frequentist parameter estimates. Best-fit parameter estimates refer to the maximum likelihood parameter values, while the 68% confidence level (CL) is given by  $-2\Delta \ln \mathcal{L} = 1$ . Upper limits are quoted at 95% CL, i.e. given by  $-2\Delta \ln \mathcal{L} = 2.71$ , referring to single-sided upper limits. The energy bins (i)-(iii) as defined in Section III were analyzed separately.

Figures 3 and 4 depict the profile likelihood functions for the  $A_{\text{DM}}$  parameter (together with the statistical distributions expected for the null hypothesis), given DM setups which are exemplary for the results discussed in the following sections.

#### A. Source-count Distribution $dN/dS$

The  $dN/dS$  distribution was parameterized with an MBPL with three free consecutive breaks. Correspondingly, the MBPL contributes 8 degrees of freedom in total, i.e. 4 power-law indexes and a normalization constant in addition to the break positions. The fitted  $dN/dS$  distribution was consistent with measurements derived from the 3FGL [10] point-source catalog (see Z16a,b for details) in all analyses. As discussed in Z16a,b, the  $dN/dS$  fit obtained from the 1pPDF extends previous catalog measurements to the regime of faint, unresolved sources. All fits were sufficiently stable and converged.

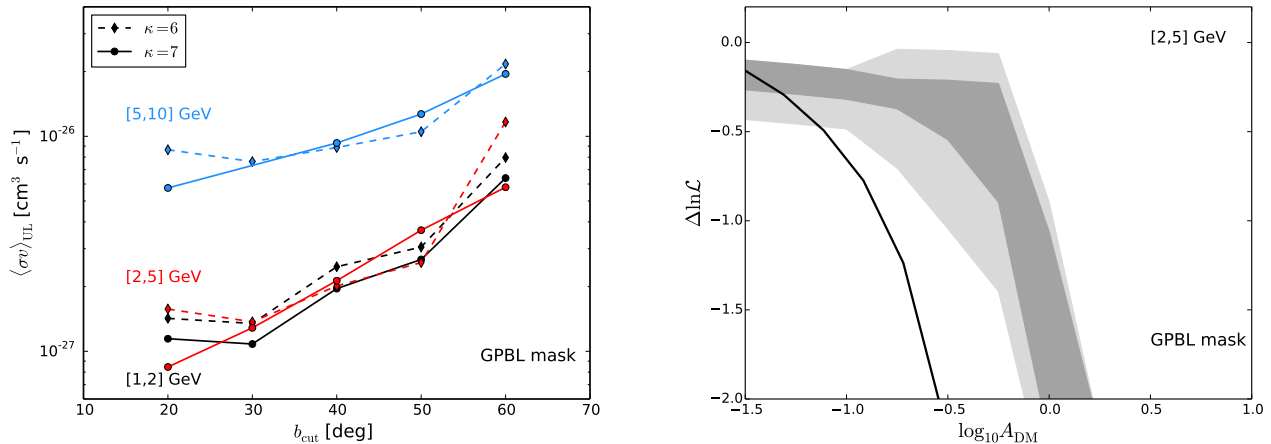


FIG. 3. Left panel: Upper limits on the DM self-annihilation cross section  $\langle\sigma v\rangle$  as function of the Galactic latitude cut  $b_{\text{cut}}$  and the pixel size. The analyzed ROI corresponds to the entire sky, excluding the GP region  $|b| < b_{\text{cut}}$ , the Fermi Bubbles, and Galactic Loop I (i.e. the GPBL mask). The limits refer to a DM mass of 15 GeV, and the  $\tau^+\tau^-$  annihilation channel. Results are shown for all three energy bands considered. The DM halo has been modeled with the Einasto profile. The dashed lines (diamonds) depict results obtained by using a HEALPix grid with order  $\kappa = 6$ , while the solid lines (circles) show limits obtained with  $\kappa = 7$ . Right panel: Statistical behavior of the ROI as analyzed in the left panel for  $b_{\text{cut}} = 30^\circ$  and  $\kappa = 7$ . The gray-shaded bands depict the 68% (darkgray) and 95% (light-gray) confidence intervals derived from the statistical scatter of the  $A_{\text{DM}}$  profile likelihood function, as obtained from simulations of the gamma-ray sky by assuming  $A_{\text{DM}} = 0$ . The solid black line shows the corresponding result obtained from the real flight data.

## B. Region of Interest Optimization

In order to produce statistically stable and robust results, the analysis was optimized with respect to the choice of the ROI and the choice of the pixel size. ROI optimization was based on two main aspects, addressed in the following paragraphs: (i) systematics related to Galactic foreground emission and (ii) statistical validity.

The DM density distribution peaks in the center of the Galactic DM halo, and thus data from the central regions of the Galaxy could have significant impact on constraining a potential DM contribution. As detailed in Section II A, it is however well known that the modeling of the strong foreground emission from the GC region is equipped with high systematic uncertainties that could significantly affect the 1pPDF. We therefore chose to mask the GC and GP emissions by excluding low Galactic latitudes  $|b| < b_{\text{cut}}$  from the ROI. Further systematics could be introduced by potential mismodelings of the Fermi Bubbles [59, 60] and Galactic Loop I [61] that were masked as well. This mask, as depicted in Fig. 2 by the gray region, will be referred to as *GPBL mask* in the remainder. We optimized the analysis setup with regard to the choice of  $b_{\text{cut}}$ .

Moreover, past studies have demonstrated that fitting diffuse templates using ROIs which cover a large fraction of the sky could potentially lead to over-subtraction issues. In particular, as discussed in Refs. [62–65], this is connected to possible mismodelings of backgrounds, namely the Galactic diffuse emission. To mitigate a possible over-subtraction of background models in our anal-

ysis, we reduced and optimized the size of the ROI, following an approach similar to Ref. [64]. In addition, we performed simulations of the gamma-ray sky in order to challenge our analysis setup against the null-hypothesis, i.e. assuming a gamma-ray sky without any DM component. Simulations were carried out such that to resemble the actual gamma-ray data as closely as possible, see Section IV C for further details. The actual flight data as well as simulated realizations of the sky were then analyzed with the 1pPDF setup, choosing the region introduced above as initial ROI. Subsequently, the ROI was systematically trimmed in longitude and latitude, until the statistical behavior of the flight data met the statistical expectation derived from data simulated for the null-hypothesis  $A_{\text{DM}} = 0$ . The trimming was symmetric in both East-West or North-South directions, respectively. We used the benchmark IEM,  $m_{\text{DM}} = 15$  GeV, and annihilation into  $\tau^+\tau^-$  for all analyses related to the optimization process. Details are discussed in the following.

As a first step, we try to identify the optimum value for the Galactic latitude cut  $b_{\text{cut}}$ , while investigating possible systematics due to the choice of the HEALPix resolution. For each energy bin, the left panel of Fig. 3 shows upper limits on  $\langle\sigma v\rangle$  as a function of the Galactic latitude cut  $b_{\text{cut}}$ . The figure displays results referring to the GPBL mask only, i.e. here we consider the almost entire extragalactic gamma-ray sky. All limits are shown for two HEALPix resolutions, i.e.  $\kappa = 6$  and  $\kappa = 7$ . As demonstrated by the figure,  $b_{\text{cut}}$  values equal or above  $\sim 30^\circ$  yield considerably stable upper limits, with

monotonically decreasing sensitivity caused by decreasing event statistics for larger  $b_{\text{cut}}$  values. Larger ROIs, corresponding to smaller values of  $b_{\text{cut}}$  below  $30^\circ$  might instead be affected by the stronger Galactic foreground morphology and should therefore be disregarded. Upper limits derived for different pixel sizes are almost equal for  $b_{\text{cut}} > 30^\circ$ , with only slight differences presumably originating from sampling effects or other small systematics. In the following, all the analyses were carried out with HEALPix resolution  $\kappa = 7$ .

As argued above, the statistical validity of the ROI was challenged with simulations of the gamma-ray sky. The right panel of Fig. 3 compares the statistical expectation for the null-hypothesis with the analysis of the actual flight data for the GPBL mask. It can be seen that the  $A_{\text{DM}}$  profile likelihood function is significantly below the statistical scatter of the simulations.

In order to find a statistically valid analysis region, the ROI was subsequently shrunk in Galactic longitude  $l$  and latitude  $b$ . Given the large extent of the Galactic Loop I structure in the Northern hemisphere, here we focussed on the study of the Southern hemisphere, where the ROI could be placed comparably closer to the GC. In particular, we studied the following ROIs: (i) stripe-shaped, e.g.  $l \in [0, 360]$  deg,  $b \in [-40, -30]$ ,  $[-50, -40]$ , and  $[-60, -50]$  deg, and (ii) box-shaped, e.g.  $l \in \{[0, 80], [280, 360]\}$  deg,  $b \in [-60, -40]$  deg. All three energy bands were considered separately. Given the systematic reduction of the ROI size in  $l$  and  $b$ , we found that real flight data match the sensitivity expected from simulations for ROIs with longitudes  $|l| < 90^\circ$  (centered on  $l = 0^\circ$ ) and  $b \in [-60, -30]$  deg.

Figure 4 compares the statistical behavior of the simulations with actual flight data for the DM\_ROI defined by  $l \in \{[0, 80], [280, 360]\}$  deg and  $b \in [-60, -40]$  deg, which we chose as benchmark ROI due to stability and robustness. It can be seen that the statistical behavior of the flight data is well consistent with the expectation. Larger ROIs (within the allowed ranges as given above) may slightly improve sensitivity by a factor of  $< 2$ . The chosen DM\_ROI is shown in Fig. 5, demonstrating the influence of the benchmark IEM in the ROI.

### C. Simulations of the Fermi Sky

Realistic Monte Carlo simulations of the gamma-ray sky were produced using the `gtoobsim` utility of the Fermi Science Tools v10r0p5, as similarly done in [33]. The considered time interval, as well as event class and energy range match the selection done for the real flight data discussed in Section III.

Three components enter the simulated counts map: point sources, Galactic foreground, and diffuse isotropic background emission. The flux distribution of point sources  $dN/dS$  was taken as the best fit to the real data (see Section IV A). For each simulation a list of point

sources was produced with a Monte Carlo simulation, with fluxes following the chosen  $dN/dS$  distribution and random positions across the sky. The flux spectrum of simulated sources was taken to be a power law, where the photon index for each source was drawn from a Gaussian distribution with mean  $\Gamma = 2.4$  and standard deviation  $\sigma_\Gamma = 0.4$ . Point sources were simulated down to fluxes of  $S_{\text{min}} = 10^{-12} \text{ cm}^{-2} \text{ s}^{-1}$ . The official diffuse Galactic emission template named `gll_iem_v06.fits` was used. For the isotropic emission, we used the recommended spectral template corresponding to our data selection, `iso_P8R2_ULTRACLEANVETO_V6_PSF3_v06.txt`. The normalization of the isotropic emission was chosen to match the integral flux  $F_{\text{iso}}$  observed in real data (see Tab. I). An effective PSF correction was computed according to the simulation properties. The resulting mock data maps were then analyzed with the same analysis chain as used for the real data, see Section III.

## V. RESULTS

Figure 6 shows the upper limits on the self-annihilation cross section  $\langle\sigma v\rangle$  of DM particles (such as WIMPs) annihilating to  $b\bar{b}$  (left panel) and  $\tau^+\tau^-$  (right panel) final states, obtained with the 1pPDF setup as developed above. The upper limits were derived using the benchmark IEM, for DM particles with masses between 5 GeV and 1 TeV. The 1pPDF analysis was performed on the DM\_ROI data. The three adjacent energy bins (i) 1.04–1.99 GeV, (ii) 1.99–5.0 GeV, and (iii) 5.0–10.4 GeV were considered to be independent from each other, yielding three different results for each annihilation channel. Using the benchmark IEM, no evidence was found for the additional DM component to significantly improve the quality of the fit, corresponding to an open, single-sided profile likelihood curve for the  $A_{\text{DM}}$  parameter (cf. Fig. 4). The different shapes of the curves for  $b\bar{b}$  and  $\tau^+\tau^-$  final states originate from the different gamma-ray emission spectra  $dN_f/dE$ , where in particular annihilation to  $b\bar{b}$  yields softer gamma-ray spectra than annihilation to  $\tau^+\tau^-$ .

For all upper bounds, we also show the 95% confidence level expected sensitivity derived from the simulations, as described in the previous section. Figure 6 compares the 1pPDF results to upper limits obtained from the stacking of several dwarf spheroidal galaxies (dSphs) [66]. We find that the sensitivity reach of the 1pPDF analysis is comparable with the analysis of dSphs, in particular for dark matter masses below 100 GeV (depending on the annihilation channel). Note that the different shape of the 1pPDF limits with respect to the dSph limits is owed to the integration over different energy intervals.

The 1pPDF fit decomposes the gamma-ray sky according to the modeling discussed in Section II A. For each energy bin, Tab. I lists the fractional contributions from the three main components to the total integral flux  $F_{\text{tot}}$ , i.e. from point sources ( $q_{\text{ps}}$ ), from the benchmark IEM



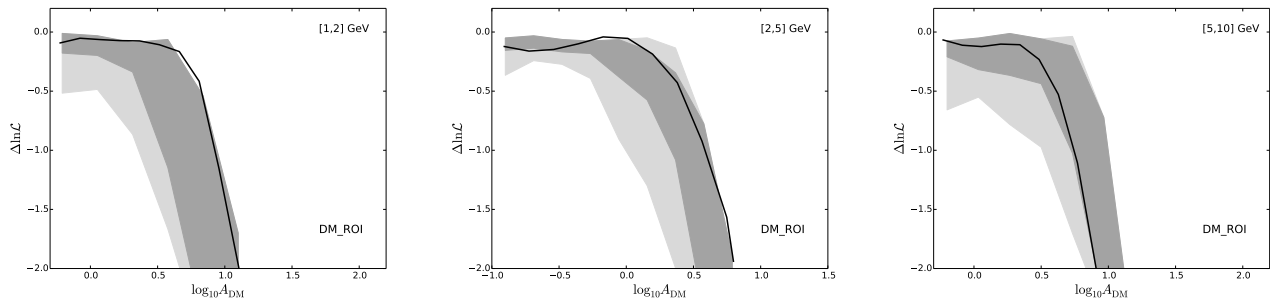


FIG. 4. Comparison of the actual flight data with the statistical expectation for the null-hypothesis as derived from simulations. The DM\_ROI (see Fig. 5) has been considered in the three energy bands 1.04–1.99 GeV (left panel), 1.99–5.0 GeV (middle panel), and 5.0–10.4 GeV (right panel). The analysis setup refers to a DM mass of 15 GeV, and the  $\tau^+\tau^-$  annihilation channel. The gray-shaded bands depict the 68% (darkgray) and 95% (light-gray) confidence intervals derived from the statistical scatter of the  $A_{\text{DM}}$  profile likelihood functions, as obtained from simulations of the gamma-ray sky by assuming  $A_{\text{DM}} = 0$ . The solid black line shows the corresponding result obtained from the actual data.

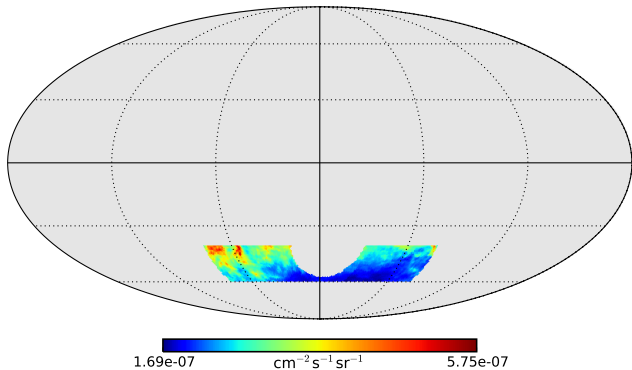


FIG. 5. The DM\_ROI considered in this analysis. The Mollweide projection depicts the benchmark IEM template in Galactic coordinates, centered on the GC. The map shows the integral flux  $F_{\text{gal}}$  between 1.99 and 5.0 GeV. The area outside the DM\_ROI has been masked in gray.

( $q_{\text{gal}}$ ), and from the diffuse isotropic background component ( $q_{\text{iso}}$ ). Given the lacking significance for a possible DM component, here its contribution is assumed to be negligible. The quantities in Tab. I refer to the 1pPDF analysis using GPBL mask. Very similar results are found using our final DM\_ROI, with larger uncertainties due to smaller statistics.

The upper limits presented in Fig. 6 were obtained for the benchmark, official *Fermi* IEM. Possible degeneracies with the IEM as a single component were incorporated by means of the normalization parameter  $A_{\text{gal}}$ . As such, the results presented in the figure reflect statistically valid upper limits under the assumption that systematic uncertainties of the IEM and its constituents are small as compared to statistical uncertainties. However, degeneracies between the DM component with particular IEM constituents, such as IC emission, remain possible.

To estimate the scatter of the upper limits with re-

TABLE I. Composition of the gamma-ray sky for  $|b| \geq 30^\circ$ . The quantities  $q_{\text{ps}}$ ,  $q_{\text{gal}}$ , and  $q_{\text{iso}}$  denote the fractional contribution from the corresponding component to the integral map flux  $F_{\text{tot}}$ . The total flux  $F_{\text{tot}}$  is given in units of  $10^{-7} \text{ cm}^{-2} \text{ s}^{-1} \text{ sr}^{-1}$ .

Component	1.04–1.99 GeV	1.99–5.0 GeV	5.0–10.4 GeV
Sources ( $q_{\text{ps}}$ )	$0.28^{+0.03}_{-0.03}$	$0.21^{+0.03}_{-0.02}$	$0.21^{+0.04}_{-0.03}$
IEM ( $q_{\text{gal}}$ )	$0.714^{+0.007}_{-0.005}$	$0.675^{+0.008}_{-0.011}$	$0.548^{+0.019}_{-0.018}$
Isotropic ( $q_{\text{iso}}$ )	$0.03^{+0.02}_{-0.01}$	$0.12^{+0.03}_{-0.04}$	$0.24^{+0.03}_{-0.05}$
$F_{\text{tot}}$	$7.828^{+0.016}_{-0.016}$	$3.875^{+0.111}_{-0.111}$	$0.951^{+0.005}_{-0.005}$

spect to the diffuse Galactic foreground emission, Fig. 7 compares the results obtained previously to upper limits derived for the selection of three other IEMs. The IEMs considered here were selected to bracket plausible Galactic foreground emission scenarios. We chose models A, B, C as discussed in Section II A. The figure depicts upper limits for DM particle masses 15, 50, and 100 GeV, considering annihilation into  $b\bar{b}$  and  $\tau^+\tau^-$ . We find that the upper limits obtained for model B are almost always the least constraining, because its IC emission component for  $|b| > 30^\circ$  is less prominent than in model A and C, thus leaving room for a larger DM contribution. The amplitude of the scatter due to the different IEMs is about a factor 2-3, depending on the energy bin, and is therefore comparable to the band of the expected sensitivity inherent to our analysis method. These upper bounds on  $\langle\sigma v\rangle$  are compared to the limits obtained from the observation of dwarf spheroidal galaxies, see Ref. [66].

## VI. CONCLUSIONS

It has recently been shown (see Z16a,b) that statistical properties of the *Fermi*-LAT photon counts map can be used to measure the composition of the gamma-ray sky at high latitudes, determining  $dN/dS$  down to fluxes



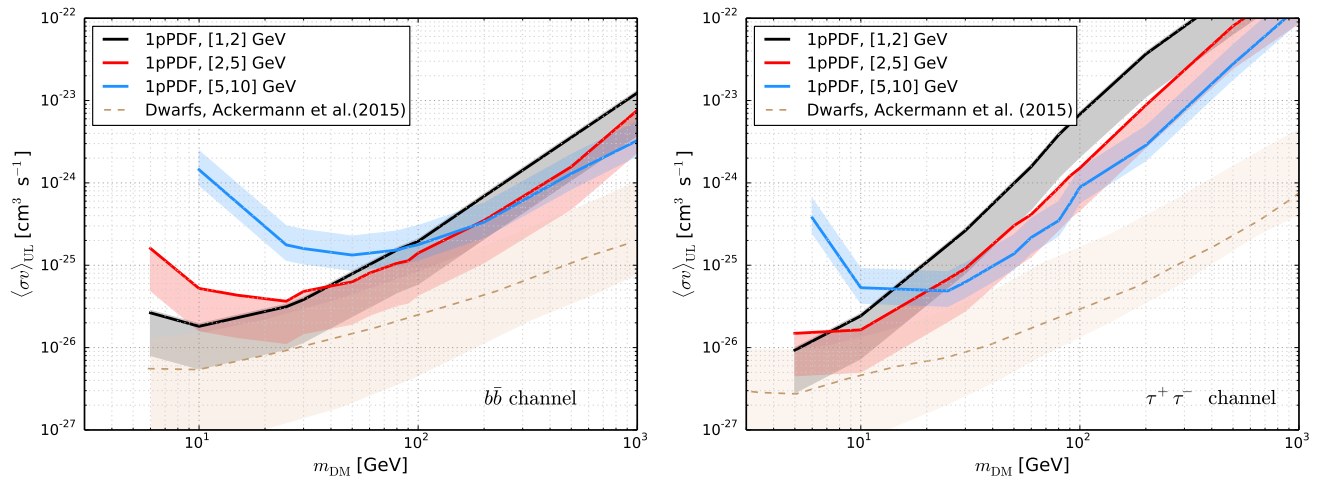


FIG. 6. Upper limits (95% CL) on the DM self-annihilation cross section  $\langle\sigma v\rangle$  as a function of the DM particle mass  $m_{\text{DM}}$ , as obtained with the 1pPDF analysis using the DM\_ROI for 8-year Fermi-LAT data (Pass 8). The DM halo of the Galaxy was assumed to follow an Einasto profile. Upper limits are given for separate analyses of the (i) 1.04–1.99 GeV (black solid line), (ii) 1.99–5.0 GeV (red solid line), and (iii) 5.0–10.4 GeV (blue solid line) energy bins. The shaded bands reflect the expected sensitivity (95% confidence level) as derived from simulations. The left (right) panel shows upper limits for total annihilation into  $b\bar{b}$  ( $\tau^+\tau^-$ ) final states. The limits are compared to recent limits obtained from the observation of dwarf spheroidal galaxies, see Ref. [66] (orange dashed line and shaded region).

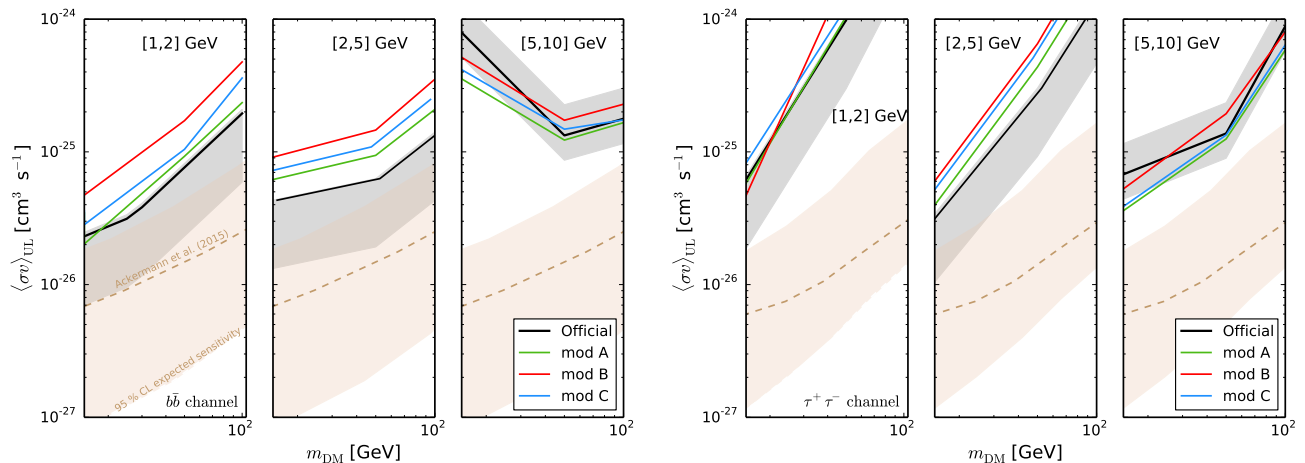


FIG. 7. Upper limits (95% CL) on the DM self-annihilation cross section  $\langle\sigma v\rangle$  for  $b\bar{b}$  (left panel) and  $\tau^+\tau^-$  (right panel) final states and  $m_{\text{DM}} = 15, 50, 100$  GeV using the DM\_ROI for 8-year Fermi-LAT data (Pass 8), obtained assuming the benchmark IEM (black solid line), model A (green solid line), model B (red solid line), and model C (blue solid line) as discussed in Section II A. The DM halo of the Galaxy was assumed to follow an Einasto profile. Upper limits are given for the three energy bins (i) 1.04–1.99 GeV (left panel), (ii) 1.99–5.0 GeV (middle panel), and (iii) 5.0–10.4 GeV (right panel). The limits are compared to the limits obtained from the observation of dwarf spheroidal galaxies, see Ref. [66] (orange dashed line). For illustrative purposes, the yellow band depicts the 95% quantile of the median expected sensitivity of the dwarf spheroidal galaxy analysis.

about one order of magnitude lower than current catalog detection limits. The high latitude gamma-ray sky is modeled with at least three components, represented by an isotropic distribution of point sources, a diffuse component of Galactic foreground emission, and diffuse isotropic background. In this paper, we have extended the photon count statistics 1pPDF method developed in

Z16a,b to a further component of the high-latitude sky, given by Galactic DM distributed in a typical smooth halo. We have employed the 1pPDF method to derive upper bounds on the possible contribution from halo DM in terms of the self-annihilation cross section  $\langle\sigma v\rangle$ , for DM masses spanning the GeV to TeV range.

We find that the 1pPDF method applied to eight years

of Pass 8 *Fermi*-LAT data at high latitudes has the sensitivity for assessing the possible gamma-ray contribution of Galactic DM annihilating into  $b\bar{b}$  or  $\tau^+\tau^-$  final states. However, we find that the analysis can be affected by over-subtraction of the background IEM when the ROI covers a significant portion of the sky. We have found that a reliable ROI for the DM analysis is a small box of the sky located in the southern hemisphere (DM\_ROI). Given the official *Fermi*-LAT interstellar emission model, the upper bounds obtained for  $\langle\sigma v\rangle$  are comparable to constraints from the stacking analysis of several dwarf spheroidal galaxies. The analysis comprises three adjacent bins in photon energy, spanning from 1 to 10 GeV. The three bins are increasingly relevant with increasing  $m_{\text{DM}}$ .

Our results have been verified against sky simulations realized with the Fermi science tools, without DM templates. The 1pPDF analysis provides results coherent with the expected sensitivity derived from the simulations, once the ROI is properly optimized. Pixelizing the sky map with different resolutions provides stable results.

Eventually, we have repeated our analysis for three additional IEM templates. The modeling of the Galactic diffuse emission has a non-negligible systematic impact, given that the upper bound on  $\langle\sigma v\rangle$  can vary by a factor of a few, depending on the energy bin and the DM mass. Using the *Fermi*-LAT official template provides stronger bounds than the models including smaller IC emission at high latitudes. This is expected, given the possible

degeneracy between IC and halo DM maps.

We have demonstrated that the method of 1-point photon count statistics, when applied to eight years of *Fermi*-LAT data, has the sensitivity for assessing a possible DM contribution to the high latitude sky down to DM self-annihilation cross section  $\langle\sigma v\rangle$  comparable to the ones bound by the currently most powerful, complementary methods.

## ACKNOWLEDGMENTS

We warmly thank A. Cuoco, N. Fornengo, D. Malyshch, and M. Regis, and SM warmly thanks M. Di Mauro and E. Charles, for useful discussions and insights. We thank the anonymous referee for their thorough check of our results and very helpful comments. SM gratefully acknowledges support by the NASA *Fermi* Guest Investigator Program 2016 through the *Fermi* one-year Program N. 91245 (P.I. M. Di Mauro), support by the Academy of Science of Torino through the *Angiola Agostinelli Gili* 2016 scholarship, and the KIPAC institute at SLAC for the kind hospitality, where a part of this project was completed. HSZ gratefully acknowledges the Istituto Nazionale di Fisica Nucleare (INFN) for a post-doctoral fellowship in theoretical physics on "Astroparticle, Dark Matter and Neutrino Physics", awarded under the INFN Fellowship Programme 2015.

- 
- [1] W. B. Atwood, A. A. Abdo, M. Ackermann, W. Althouse, B. Anderson, *et al.*, *ApJ* **697**, 1071 (2009), arXiv:0902.1089 [astro-ph.IM].
- [2] M. Ackermann, M. Ajello, A. Albert, A. Allafort, W. B. Atwood, *et al.*, *ApJS* **203**, 4 (2012), arXiv:1206.1896 [astro-ph.IM].
- [3] M. Fornasa and M. A. Sánchez-Conde, *Phys. Rep.* **598**, 1 (2015).
- [4] M. Ackermann, M. Ajello, A. Albert, W. B. Atwood, L. Baldini, *et al.*, *ApJ* **799**, 86 (2015).
- [5] Y. Inoue and T. Totani, *ApJ* **702**, 523-536 (2009), arXiv:0810.3580.
- [6] M. Ackermann, M. Ajello, A. Allafort, E. Antolini, W. B. Atwood, *et al.*, *ApJ* **743**, 171 (2011), arXiv:1108.1420 [astro-ph.HE].
- [7] K. N. Abazajian, S. Blanchet, and J. P. Harding, *Phys. Rev. D* **84**, 103007 (2011), arXiv:1012.1247.
- [8] M. Ajello, M. S. Shaw, R. W. Romani, C. D. Dermer, L. Costamante, O. G. King, W. Max-Moerbeck, A. Readhead, A. Reimer, J. L. Richards, and M. Stevenson, *ApJ* **751**, 108 (2012), arXiv:1110.3787.
- [9] J. Singal, V. Petrosian, and M. Ajello, *ApJ* **753**, 45 (2012), arXiv:1106.3111.
- [10] F. Acero, M. Ackermann, M. Ajello, A. Albert, W. B. Atwood, *et al.*, *ApJS* **218**, 23 (2015).
- [11] F. Massaro, D. J. Thompson, and E. C. Ferrara, *The Astronomy and Astrophysics Review* **24**, 2 (2015).
- [12] Y. Inoue, *ApJ* **733**, 66 (2011), arXiv:1103.3946 [astro-ph.HE].
- [13] M. Di Mauro, F. Donato, G. Lamanna, D. A. Sanchez, and P. D. Serpico, *ApJ* **786**, 129 (2014), arXiv:1311.5708 [astro-ph.HE].
- [14] M. Di Mauro, F. Calore, F. Donato, M. Ajello, and L. Latronico, *ApJ* **780**, 161 (2014), arXiv:1304.0908 [astro-ph.HE].
- [15] F. Calore, M. Di Mauro, and F. Donato, *ApJ* **796**, 14 (2014), arXiv:1406.2706 [astro-ph.HE].
- [16] I. Tamborra, S. Ando, and K. Murase, *J. Cosmology Astropart. Phys.* **9**, 043 (2014), arXiv:1404.1189 [astro-ph.HE].
- [17] M. Ajello, D. Gasparrini, M. Sánchez-Conde, G. Zaharijas, M. Gustafsson, *et al.*, *ApJ* **800**, L27 (2015), arXiv:1501.05301 [astro-ph.HE].
- [18] P. Ullio, L. Bergstrom, J. Edsjo, and C. G. Lacey, *Phys. Rev. D* **66**, 123502 (2002), arXiv:astro-ph/0207125 [astro-ph].
- [19] K. N. Abazajian, S. Blanchet, and J. P. Harding, *Phys. Rev. D* **85**, 043509 (2012), arXiv:1011.5090 [hep-ph].
- [20] M. Papucci and A. Strumia, *JCAP* **1003**, 014 (2010), arXiv:0912.0742 [hep-ph].
- [21] M. Cirelli, P. Panci, and P. D. Serpico, *Nuclear Physics B* **840**, 284 (2010), arXiv:0912.0663.
- [22] T. Bringmann, F. Calore, M. Di Mauro, and F. Donato, *Phys. Rev. D* **89**, 023012 (2014), arXiv:1303.3284 [astro-ph.CO].
- [23] M. Di Mauro and F. Donato, *Phys. Rev. D* **91**, 123001

- (2015), arXiv:1501.05316 [astro-ph.HE].
- [24] M. Ackermann *et al.* (Fermi-LAT), JCAP **1509**, 008 (2015), arXiv:1501.05464 [astro-ph.CO].
- [25] S. Dodelson, A. V. Belikov, D. Hooper, and P. Serpico, Phys. Rev. D **80**, 083504 (2009), arXiv:0903.2829 [astro-ph.CO].
- [26] S. K. Lee, S. Ando, and M. Kamionkowski, J. Cosmology Astropart. Phys. **7**, 007 (2009), arXiv:0810.1284.
- [27] D. Malyshev and D. W. Hogg, ApJ **738**, 181 (2011).
- [28] M. R. Feyereisen, S. Ando, and S. K. Lee, J. Cosmology Astropart. Phys. **9**, 027 (2015), arXiv:1506.05118.
- [29] A. Massari, E. Izaguirre, R. Essig, A. Albert, E. Bloom, and G. A. Gómez-Vargas, Phys. Rev. D **91**, 083539 (2015), arXiv:1503.07169 [hep-ph].
- [30] M. Selig, V. Vacca, N. Oppermann, and T. A. Enßlin, A&A **581**, A126 (2015).
- [31] S. K. Lee, M. Lisanti, B. R. Safdi, T. R. Slatyer, and W. Xue, Physical Review Letters **116**, 051103 (2016).
- [32] M. Lisanti, S. Mishra-Sharma, L. Necib, and B. R. Safdi, ApJ **832**, 117 (2016).
- [33] H.-S. Zechlin, A. Cuoco, F. Donato, N. Fornengo, and A. Vittino, ApJS **225**, 18 (2016).
- [34] H.-S. Zechlin, A. Cuoco, F. Donato, N. Fornengo, and M. Regis, ApJ **826**, L31 (2016).
- [35] M. Wolleben, Astrophys. J. **664**, 349 (2007), arXiv:0704.0276 [astro-ph].
- [36] M. Ackermann *et al.* (Fermi-LAT), Astrophys. J. **793**, 64 (2014), arXiv:1407.7905 [astro-ph.HE].
- [37] M. Ackermann, M. Ajello, W. B. Atwood, L. Baldini, G. Barbiellini, *et al.*, ApJ **761**, 91 (2012), arXiv:1205.6474 [astro-ph.CO].
- [38] E. Charles *et al.* (Fermi-LAT), Phys. Rept. **636**, 1 (2016), arXiv:1605.02016 [astro-ph.HE].
- [39] F. Acero, M. Ackermann, M. Ajello, A. Albert, L. Baldini, *et al.*, ApJS **223**, 26 (2016), arXiv:1602.07246 [astro-ph.HE].
- [40] M. Ackermann, M. Ajello, W. B. Atwood, L. Baldini, J. Ballet, *et al.*, ApJ **750**, 3 (2012), arXiv:1202.4039 [astro-ph.HE].
- [41] R. Catena and P. Ullio, JCAP **1008**, 004 (2010), arXiv:0907.0018 [astro-ph.CO].
- [42] J. I. Read, J. Phys. **G41**, 063101 (2014), arXiv:1404.1938 [astro-ph.GA].
- [43] H.-S. Zechlin, M. V. Fernandes, D. Elsässer, and D. Horns, A&A **538**, A93 (2012), arXiv:1111.3514 [astro-ph.HE].
- [44] M. Ackermann, A. Albert, L. Baldini, J. Ballet, G. Barbiellini, *et al.*, ApJ **747**, 121 (2012), arXiv:1201.2691 [astro-ph.HE].
- [45] H.-S. Zechlin and D. Horns, J. Cosmology Astropart. Phys. **11**, 050 (2012), arXiv:1210.3852 [astro-ph.HE].
- [46] B. Bertoni, D. Hooper, and T. Linden, J. Cosmology Astropart. Phys. **12**, 035 (2015), arXiv:1504.02087 [astro-ph.HE].
- [47] D. Schoonenberg, J. Gaskins, G. Bertone, and J. Dieemand, J. Cosmology Astropart. Phys. **5**, 028 (2016), arXiv:1601.06781 [astro-ph.HE].
- [48] D. Hooper and S. J. Witte, J. Cosmology Astropart. Phys. **4**, 018 (2017), arXiv:1610.07587 [astro-ph.HE].
- [49] F. Calore, V. De Romeri, M. Di Mauro, F. Donato, and F. Marinacci, Phys. Rev. **D96**, 063009 (2017), arXiv:1611.03503 [astro-ph.HE].
- [50] J. Einasto, Trudy Astrofizicheskogo Instituta Alma-Ata **5**, 87 (1965).
- [51] T. Bringmann and C. Weniger, Phys. Dark Univ. **1**, 194 (2012), arXiv:1208.5481 [hep-ph].
- [52] M. Cirelli, G. Corcella, A. Hektor, G. Hütsi, M. Kadastik, P. Panci, M. Raidal, F. Sala, and A. Strumia, J. Cosmology Astropart. Phys. **3**, 051 (2011), arXiv:1012.4515 [hep-ph].
- [53] *Fermi*-LAT data are publicly available at <https://heasarc.gsfc.nasa.gov/FTP/fermi/data/lat/weekly/photon/>.
- [54] <https://fermi.gsfc.nasa.gov/ssc/data/analysis/software/>.
- [55] K. M. Górski, E. Hivon, A. J. Banday, B. D. Wandelt, F. K. Hansen, M. Reinecke, and M. Bartelmann, ApJ **622**, 759 (2005), astro-ph/0409513.
- [56] F. Feroz and M. P. Hobson, MNRAS **384**, 449 (2008), arXiv:0704.3704.
- [57] F. Feroz, M. P. Hobson, and M. Bridges, MNRAS **398**, 1601 (2009), arXiv:0809.3437.
- [58] W. A. Rolke, A. M. López, and J. Conrad, Nuclear Instruments and Methods in Physics Research A **551**, 493 (2005), physics/0403059.
- [59] M. Su, T. R. Slatyer, and D. P. Finkbeiner, ApJ **724**, 1044 (2010), arXiv:1005.5480 [astro-ph.HE].
- [60] M. Ackermann, A. Albert, W. B. Atwood, L. Baldini, J. Ballet, *et al.*, ApJ **793**, 64 (2014), arXiv:1407.7905 [astro-ph.HE].
- [61] J.-M. Casandjian, I. Grenier, and for the Fermi Large Area Telescope Collaboration, ArXiv e-prints (2009), arXiv:0912.3478 [astro-ph.HE].
- [62] T. Daylan, D. P. Finkbeiner, D. Hooper, T. Linden, S. K. N. Portillo, N. L. Rodd, and T. R. Slatyer, Phys. Dark Univ. **12**, 1 (2016), arXiv:1402.6703 [astro-ph.HE].
- [63] F. Calore, I. Cholis, and C. Weniger, JCAP **1503**, 038 (2015), arXiv:1409.0042 [astro-ph.CO].
- [64] T. Cohen, K. Murase, N. L. Rodd, B. R. Safdi, and Y. Soreq, Phys. Rev. Lett. **119**, 021102 (2017), arXiv:1612.05638 [hep-ph].
- [65] T. Linden, N. L. Rodd, B. R. Safdi, and T. R. Slatyer, Phys. Rev. **D94**, 103013 (2016), arXiv:1604.01026 [astro-ph.HE].
- [66] M. Ackermann, A. Albert, B. Anderson, W. B. Atwood, L. Baldini, *et al.*, Physical Review Letters **115**, 231301 (2015), arXiv:1503.02641 [astro-ph.HE].